Decoupled Control of Thrust and Normal Forces of Linear Induction Motor for a Novel Magnetically Levitated System

Anton J.D. Verdel

Abstract— **This paper presents a feasibility study of a novel magnetic levitation system through the use of linear induction motor (LIM) segments implemented in a rotating ring system. Firstly, this means finding the best manner of simultaneous and decoupled control of thrust and normal forces generated by the single-sided LIM (SLIM). Secondly, an analysis is performed considering the necessity and advantage of the usage of external magnetic levitation units together with the SLIM segments, taking into account the total system architecture. Finally, this study concludes with the design and construction of a static test setup, from which the measurement results are compared and verified with analytical and numerical models.**

Index Terms— **LIM, Decoupled Control, Magnetic Levitation, Magnetic Bearing, Longitudinal End Effect, Transverse Edge Effect, Saturation, Skin Effect.**

I. INTRODUCTION

MAGNETIC suspension systems minimize mechanical friction, wear, noise and vibrations which extend the lifetime of a machine. The rotating ring system is levitated and rotated through the use of SLIMs. Which means that simultaneous and decoupled control of thrust and normal forces of the SLIM is necessary to achieve for such a system. Available publications about LIMs are very diverse and mostly written for a particular LIM with a specific operation. This shows the importance of an analytical model that corresponds with the SLIM under investigation, in our case the three phase double-layer secondary flat SLIM. A good representation of reality demands an analytical model that, besides giving a clear derivation of thrust and normal forces, particularly takes into account the following four effects: longitudinal end effect, transverse edge effect, saturation and skin effects.

A. Literature Study

Publications found about vector controlled LIMs [1]–[6] are not sufficient enough to build an analytical model from, none of these six papers includes all pre-described four parasitic effects.

The next set of papers [7]–[10] discusses various ways of decoupling the thrust and normal forces simultaneously. A

control method of thrust and normal forces using the combined power source, which has a low frequency and a high frequency component, is proposed in [7]. The low frequency component is used to control thrust force and supports the weight of the system, and the high frequency component is used to control the normal force. Another method [8] shows how the slip frequency can be determined uniquely from dividing the thrust force F_t by the normal force F_n according to $F_t/F_n = function(f_{slip})$. From the unique slip frequency, the reference thrust force and the air gap length, the primary current and the power supply frequency of the LIM can be derived.

Yamamura [11] extensively discusses the double-sided secondary flat LIM with longitudinal end effects. The difference between the single-layer and double-layer secondary lies in the secondary back iron. Because Yamamura's model does not consist of a secondary back iron no saturation is derived. Also the transverse edge effect is not implemented in his model.

Two analytical models have been chosen to be implemented and executed for the performance calculation of the SLIM. The first one is based on the theory of Gieras [12]–[14], the other one on the theory of Boldea & Nasar [15] and [16]. Both theoretical approaches provide solutions for the longitudinal end effects, transverse edge effects, skin effects and saturation. Both theories are applicable, because they are developed for the same double-layer secondary flat SLIM.

B. Structure

The specifications and characteristics of the SLIM under investigation are described in Section II. The two analytical models, followed by a numerical model of the SLIM are respectively discussed in Sections III and IV. Section V describes the measurement setup, and Section VI shows the results of the measurements and validates them with the results of the analytical and numerical models. Finally, Section VII gives the system architecture of whole the rotating ring system followed by the overall conclusions and recommendations in Section VIII.

II. SPECIFICATIONS OF THE SLIM

The arc-shaped SLIM consists of a fixed primary and a moving secondary. Fig. 1 shows the arc-shaped primary without windings. The primary teeth and back iron are made of 0.35 mm iron silicon laminated material M235-35A, and has a pack of 200 laminations to prevent major influence of

eddy currents in the primary. Increasing the number of poles will improve the force capability, however, it also increases the manufacturing complexity and, therefore, rises the cost of a SLIM segment. Among these design criteria a trade-off has been made; the SLIM is constructed with 4 pole pairs.
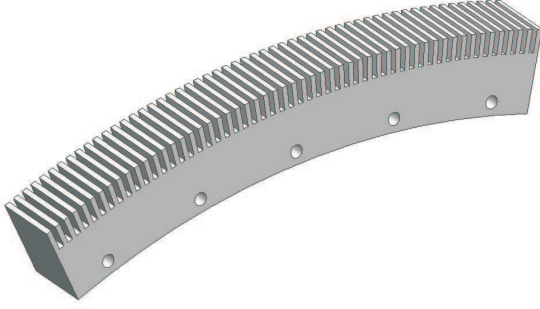

Fig. 1.   Arc-shaped primary in 3D drawn model shown without the windings.

The primary windings are shown in Figs. 2(a) and 2(b). One should notice the double layer of windings in Fig. 2(a) which improves the magnetic flux distribution and reduces the resistance and leakage reactance significantly. Also the half end slots at both ends of the primary can be seen, it is $5/6$ short pitched to eliminate the 5th and 7th order harmonics of the induced magnetic flux density, which is a major disturbance [17]. The total width of the primary is given by the primary core width L_{prim} of 70 mm and the width of end windings which is 50 mm, this sums up to a total width of 120 mm. The secondary of the SLIM consists of a non-ferromagnetic
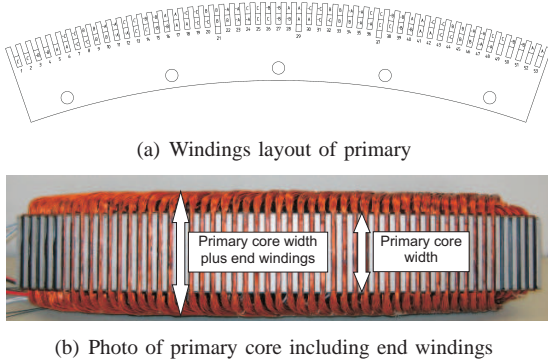

(a) Windings layout of primary

(b) Photo of primary core including end windings

Fig. 2.   Primary windings shown (a) in setup with double layer windings, half filled end slots and $5/6$ short pitched windings and (b) the primary core including end windings.

high conductive Aluminum T633/80[1] layer backed up with a ferromagnetic steel[2] core. To produce a high magnetic flux density from a certain amount of current it is important to keep the height of the air gap g as small as possible, therefore it is set at 1 mm.

Table I gives all the parameters and dimensions of the primary and the secondary of the SLIM under investigation. The total length of the primary equals a length according to

---

[1]Also known as AlSi1MgMn.
[2]Also known as 11SMn28.

TABLE I

PARAMETERS AND DIMENSIONS OF THE PRIMARY AND SECONDARY CHARACTERIZING THE SLIM

Primary	symbol	value	unit
Number of turns	N	ref. [17]	–
Number of pole pairs	p	4	–
Number of phases	m_{ph}	3	–
Number of slots per phase per pole	$NSPP$	2	–
Coil pitch	θ_c	$(5/6)\pi$	rad
Pole pitch	τ	ref. [17]	mm
Height of primary back iron	h_{prim}	ref. [17]	mm
Height of teeth	h_t	ref. [17]	mm
Height of slot	h_{slot}	ref. [17]	mm
Width of teeth	w_t	ref. [17]	mm
Width of slot	w_{slot}	ref. [17]	mm
Primary core width	L_{prim}	70	mm
Radius of primary	r	800	mm
Phase resistance	R_{ph}	1 ± 0.1	Ω
Phase inductance	L_{sl}	4.6 ± 0.5	mH
Relative magnetic permeability of M235-35A	μ_{M235}	$B - H$ curve	–
Secondary			
Height of Aluminium layer	d	ref. [17]	mm
Height of secondary back iron	h_{sec}	ref. [17]	mm
Width of secondary back iron	w_{sec}	80	mm
Width of overhang	w_{ov}	$-2.5 \,\&\, 0$	mm
Relative magnetic permeability of T633/80	μ_{Al}	1.01	–
Relative magnetic permeability of N100	μ_{N100}	$B - H$ curve	–
Conductivity of T633/80	σ_{Al}	$27 \cdot 10^6$	S/m
Conductivity of N100	σ_{N100}	$5 \cdot 10^6$	S/m

$[\tau(2p + 5/6) + w_t]$. The width overhang w_{ov} is given for two values because the secondary is tested with two Aluminum layer widths, Fig. 3(b) illustrates w_{ov}. A negative value of w_{ov} means that the Aluminum layer width is shorter than the secondary back iron width w_{sec}. The phases of the primary are WYE-connected and the three phase currents are given by:

$$i_A = \sqrt{2}I_{prim}\cos(\omega t), \tag{1a}$$

$$i_B = \sqrt{2}I_{prim}\cos(\omega t + 2\pi/3), \tag{1b}$$

$$i_C = \sqrt{2}I_{prim}\cos(\omega t - 2\pi/3). \tag{1c}$$

III. ANALYTICAL MODELS

The main advantage of an analytical model is its fast computational processing time, also the ease of adjusting variables and parameters with direct result contributes to its success.

The two implemented analytical models are based on theoretical approaches of Gieras [12]–[14] and Boldea & Nasar [15] and [16]. Both models are implemented in Mathcad software and contain the derivation of thrust and normal forces and the following effects:

- longitudinal end effect,
- transverse edge effect,
- skin effect,
- magnetic saturation.

This section discusses the most important equations per model, for complete derivation of the formulas one is referred to [18]. Figure 3 shows two schematic drawings with parameters of the

(a) 3D schematic drawing of SLIM with parameters [14]

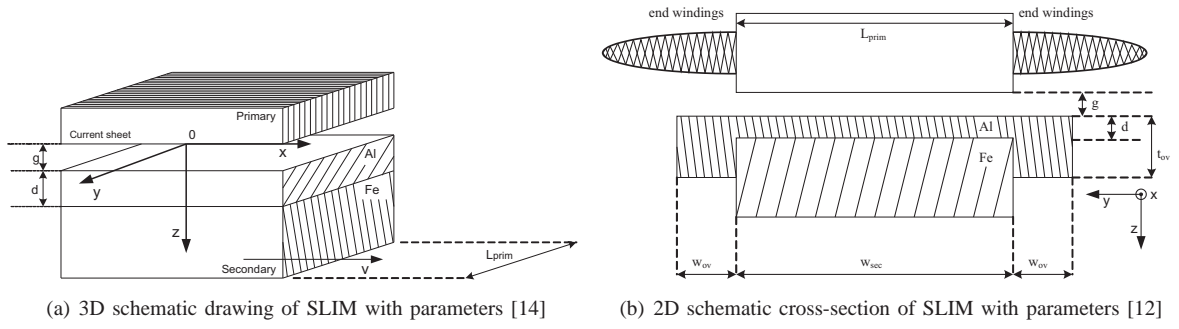(b) 2D schematic cross-section of SLIM with parameters [12]

Fig. 3.   SLIM parameters given by (a) 3D schematic drawing and (b) 2D schematic cross-section.

SLIM which are convenient during the derivation of the force equations. The upcoming equations (2-5) are the same for both analytical models, the equivalent air gap g_c is given by:

$$g_c = g\frac{k_C(g+d)g + d^2 - gd}{g^2 + d^2}, \qquad (2)$$

$$k_C = \frac{t_1}{t_1 - \gamma g_t}, \qquad (3)$$

$$\gamma = \frac{4}{\pi}\left\{\frac{w_{slot}}{2g_t}\arctan\frac{w_{slot}}{2g_t} - \ln\sqrt{1 + \left(\frac{w_{slot}}{2g_t}\right)^2}\right\}, \qquad (4)$$

$$g_t = g + d, \qquad (5)$$

with k_C-the Carter coefficient, t_1-the primary slot pitch, g_t-the total resultant air gap and γ-empirical coefficient.

A. Gieras Model

The approach of Gieras is based on a solution of the two-dimensional (2D) electromagnetic field distribution.

1) Longitudinal End Effect: To implement the longitudinal end effect two assumptions have to be made; the three-phase supply voltages are balanced and the primary winding is replaced by an equivalent current sheet, in which the complex amplitude is given by:

$$A_{m\nu} = \frac{m_{ph}\sqrt{2}I_{prim}Nk_{w\nu}}{p\tau}\exp\left[j(\nu-1)\frac{m_{ph}-1}{m_{ph}}\right], \quad (6)$$

where I_{prim} is the root-mean-square (RMS) primary current and $k_{w\nu}$ is the primary winding factor for the νth-space harmonic. The longitudinal end effect factor k_e is calculated according to:

$$k_e = \frac{E_{me}}{E_{ms}}, \qquad (7)$$

where E_{ms} is the peak value of the EMF induced in the primary phase winding by the magnetic flux density wave with synchronous velocity, and E_{me} is the peak value of EMF induced by the damped entry-end wave. The end effect factor k_e is implemented in (19).

2) Transverse Edge Effect: The transverse edge effect is due to the finite width of the SLIM and implemented via an appropriate decrease in conductivity of the secondary according to (8):

$$\sigma'_{Al} = k_{RN}\sigma_{Al}. \qquad (8)$$

The Russel and Norsworthy modified coefficient k_{RN} for the νth-harmonic is:

$$k_{RN} = 1 - \frac{\tanh\frac{\beta_\nu w_{sec}}{2}}{(\frac{\beta_\nu w_{sec}}{2})[1 + k_t\tanh\frac{\beta_\nu w_{sec}}{2}\tanh\beta_\nu w_{ov}]}, \quad (9)$$

where β_ν is the real constant dependent on the space harmonic order and k_t-an empirically found constant depending on the thickness of overhang t_{ov}. Finally, we have to implement the transverse edge effects into the secondary solid steel layer, this is done by increasing the secondary impedance with coefficient $k_{z\nu}$:

$$k_{z\nu} = 1 - \frac{g}{\nu L_{prim}} + \frac{2}{\nu\pi}\frac{\tau}{w_{sec}}\left[1 - \exp\left(-\nu\frac{\pi}{2}\frac{w_{sec}}{L_{prim}}\right)\right]. \qquad (10)$$

3) Saturation: The saturation factor of the magnetic circuit for the SLIM is defined as:

$$k_\mu = \frac{V_\nu}{2V_{g\nu} + 2V_{d\nu}}, \qquad (11)$$

with V_ν-the MMF due to the νth-harmonic per pole pair, $V_{g\nu}$-the magnetic potential drop across the air gap and $V_{d\nu}$-the magnetic potential drop across the Aluminum layer.

4) Impedance: The air gap mutual reactance and the leakage reactance are respectively given by:

$$X_{\nu 0} = 4m_{ph}\frac{\omega}{2\pi}\mu_0\frac{(Nk_{w\nu})^2}{\nu p}\frac{L_{prim}}{\beta_\nu g_c k_\mu}, \qquad (12)$$

$$X_{sl} = 4\pi\frac{\omega}{2\pi}\mu_0\frac{N^2}{pNSPP}L_{prim}\frac{h_t}{3w_t}. \qquad (13)$$

The resultant impedance, referred to the primary winding, of the double-layer reaction rail for the νth-space harmonic is:

$$Z'_{2\nu} = \frac{Z'_{\nu Al}Z'_{\nu Fe}}{Z'_{\nu Al} + Z'_{\nu Fe}}\frac{1}{s_\nu}, \qquad (14)$$

with

$$s_\nu = 1 - \nu(1-s), \qquad (15)$$

where s denotes slip and s_ν-harmonic dependent slip.

Now it is easy to derive the secondary resistance $R'_{2\nu}$ and secondary reactance $X'_{2\nu}$:

$$R'_{2\nu} = Re(Z'_{2\nu}), \qquad (16)$$

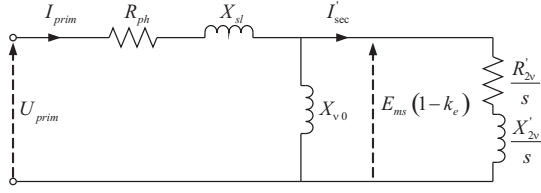$$X'_{2\nu} = Im(Z'_{2\nu}). \qquad (17)$$

Fig. 4.   Per phase equivalent circuit of the SLIM according to Gieras [12].

5) Force: The thrust force F_t is derived, with help of Fig. 4, from the primary and secondary current with the longitudinal end effect factor according to:

$$E_{ms} = I_{prim} \frac{1}{\left(\frac{1}{Z'_{2\nu}} + \frac{1}{jX_{\nu 0}} \right)}, \tag{18}$$

$$I'_{sec} = (1 - k_e) \frac{E_{ms}}{Z'_{2\nu}}, \tag{19}$$

$$F_t = \frac{m_{ph} \left(I'_{sec} \right)^2 R'_{2\nu}}{s v_s}. \tag{20}$$

The normal force F_n is the subtraction of the attractive force F_{na} and the repulsive eddy current reaction force F_{nr} given by:

$$F_n = F_{na} - F_{nr}. \tag{21}$$

The repulsive eddy current reaction force F_{nr} increases simultaneously with an increase in slip frequency, which means that the total net normal force F_n decreases. Finally, the attractive and repulsive forces are:

$$F_{na} = \frac{B_{zg}^2}{4\mu_0} A, \tag{22}$$

$$F_{nr} = F_t \frac{B_{xg}}{B_{zg}}, \tag{23}$$

with, respectively, B_{xg}- and B_{zg}-the air gap magnetic flux density in the x- and z-direction, A represents the active surface of the primary core.

B. Boldea & Nasar Model

This approach neglects the core losses and at rated frequency the skin effect is small, therefore $X'_2 \approx 0$. One should notice the mechanical power and the secondary loss, respectively represented by resistances R'_m and R'_2 in Fig. 5, to take into account the longitudinal end effect. The quasi-one-
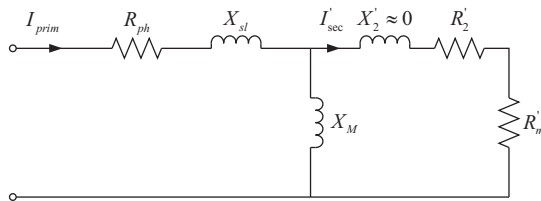

Fig. 5.   Per phase equivalent circuit of the SLIM according to Boldea & Nasar [15].

dimensional theory includes the transverse edge effect, skin effect and secondary saturation by means of appropriate co-efficients, implemented by equivalent secondary conductivity σ_e and equivalent gap g_e. This model only takes into account the fundamental space harmonic, so the primary current sheet of (6) becomes:

$$J_m = \frac{m_{ph} \sqrt{2} I_{prim} N k_w}{p\tau}. \tag{24}$$

1) Saturation: From the skin depth in the Aluminum layer d_s and the depth of penetration in the secondary back iron δ_i one can respectively derive the skin effect factor K_{sk} and back iron saturation factor K_s:

$$K_{sk} = \frac{2d}{d_s} \left(\frac{\sinh \left(\frac{2d}{d_s} \right) + \sin \left(\frac{2d}{d_s} \right)}{\cosh \left(\frac{2d}{d_s} \right) - \cos \left(\frac{2d}{d_s} \right)} \right), \tag{25}$$

$$K_s = \frac{\mu_0}{\mu_{N100} \delta_i g_t k_C k^2}, \tag{26}$$

with k-the equivalent wave number.

2) Transverse Edge Effect: The transverse edge effect is implemented by the equivalent secondary conductivity given by:

$$\sigma_e = \frac{\sigma_{Al}}{K_{sk}} \frac{K_{iron}}{K_{tr}}, \tag{27}$$

where K_{iron} denotes the iron factor and K_{tr} the transverse edge effect for Aluminum.

3) Longitudinal End Effect: K_{Fx} represents the longitudinal end effect factor, given by:

$$K_{Fx} = \frac{F_t v_s}{P_2 + P_m}. \tag{28}$$

The secondary losses P_2, the total electromagnetic power P_m and the thrust force F_t, which is given in (34), strongly depend on the equivalent gap g_e:

$$g_e = \frac{g_t k_C K_l (1 + K_s)}{K_{mt}}, \tag{29}$$

with K_l-the air gap leakage factor and K_{mt}-a transverse edge effect coefficient.

4) Impedance: The magnetizing inductance M', the loss producing resistance R'_2 and the mechanical power producing resistance R'_m are given by:

$$M' = \frac{2W_m}{3I_{prim}^2} \left(1 + \frac{1}{y^2} \right), \tag{30}$$

$$R'_2 = \frac{P_2}{3I_{prim}^2} (1 + y^2), \tag{31}$$

$$R'_m = \frac{P_m}{3I_{prim}^2} (1 + y^2), \tag{32}$$

with

$$y = \frac{2\omega W_m}{P_2 + P_m}, \tag{33}$$

where W_m stands for the total magnetic stored energy.

5) Force: Finally, the thrust force F_t and normal force F_n are calculated according to:

$$F_t = \mu_0 a_e J_m \frac{1}{k} Re \left[A_2^* \frac{(\exp[(\gamma_2^* - j)k2p\tau] - 1)}{\gamma_2^* - j} + H_n^* k2p\tau \right],$$
(34)

$$F_n = \frac{W_m}{g_e} + a_e \mu_0 g_e Re \left[\int_0^{2p\tau} J_m \exp[jkx] \frac{\partial H_r}{\partial x} \, dx \right], \quad (35)$$

where a_e is the equivalent width, A_2-the air gap magnetic vector potential, γ_2-the air gap field propagation constant, H_n-the conventional air gap field, H_r-the air gap reaction field and, finally, $*$-the conjugate value.

IV. NUMERICAL MODEL

Numerical models have been made with finite element (FE) program OPERA-2D. The finite element method (FEM) solves the partial differential equations that describe the behavior of the electromagnetic fields. The FE analysis program iteratively determines the correct solution including non-linear effects, if these are modeled. Numerical errors due to coarse mesh definition are also defined so that mesh can be redefined to achieve the required accuracy. In total three modules of OPERA-2D have been used to perform the FE analysis, namely:

- ST, the Static Field program solves for time invariant magnetic and electric fields.
- AC, the steady-state AC program solves eddy current problems where driving currents are varying sinusoidally in time.
- LM, the Linear Motion program is a transient eddy current solver, extended to include the effects of motion.

Through the use of command files ($*$.comi) one can automate data input into the pre- and post processor of OPERA-2D and define models with their dimensions and parameters. This efficiently shortens the designing time when multiple simulations have to be performed.

The provided data in Table II is implemented in the 2D FEM to achieve a low linearizing error originated from the true non-linear behavior. The specifications, i.e. the dimensions and

TABLE II
2D FEM DATA

Max. number of elements	100000
Max. number of refinement iterations	21
Final convergence accuracy [%]	1
Tolerance of non-linear analysis	$1 \cdot 10^{-3}$

parameters of Table I, are implemented in OPERA-2D via the pre-processor. Figure 6(a) shows the overall drawing of the SLIM, Figs. 6(b) and 6(c) respectively illustrate the SLIM zoomed in without and with mesh. The force **F** derived from the Maxwell stress tensor in vector notation, with surface S completely enclosing the primary, is given by:

$$\mathbf{F} = \oint_S (\mathbf{B} \cdot \mathbf{n}) \frac{\mathbf{B}}{\mu_0} - \frac{1}{2} \mathbf{n} \left(\frac{\mathbf{B}^2}{\mu_0} \right) dS. \quad (36)$$
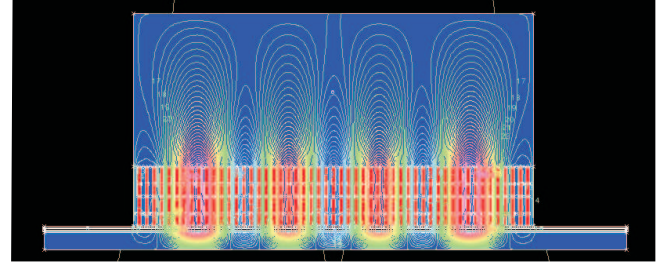
(a) SLIM overall (not in scale) with vector potential lines
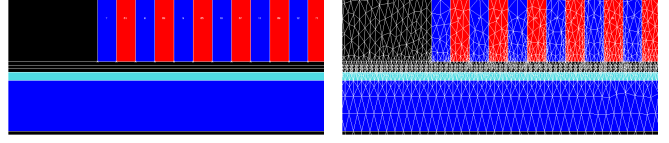
(b) zoomed in air gap   (c) zoomed in air gap with mesh

Fig. 6.   (a) The overall SLIM model, (b) the SLIM zoomed in air gap and (c) the SLIM zoomed in on air gap with mesh.

Because OPERA-2D is two dimensional FEM software package, the simplification and recomposition [19] of (36) results in:

$$F_t = \frac{1}{2\mu_0} \int_\Gamma (B_{zg} B_{xg}) dl \times L_{prim}, \quad (37)$$

$$F_n = \frac{1}{4\mu_0} \int_\Gamma (B_{zg}^2 - B_{xg}^2) dl \times L_{prim}, \quad (38)$$

with Γ-the closed integration contour around the primary.

Although OPERA-2D calculates field solutions with a pre-set accuracy, due to the 2D-environment the width of the SLIM is considered infinite during analysis. This means the transverse edge effect is excluded from the final solution. However, the transverse edge effect can be implemented [19] by altering σ_{Al} in OPERA-2D with the Russel and Norsworthy factor given by (8). The two dimensional origin introduces another error, namely, the assumption that the primary width of the SLIM is equal to the secondary width. Table I illustrates that the width of primary L_{prim} and secondary w_{sec} are different.

V. MEASUREMENT SETUP

A static test setup has been designed and constructed to acquire measurement data from the SLIM. The double layer secondary ring has a length of 1000 mm and a radius of 801 mm. The radius of the ring has been assembled by a steamroller, which introduces inaccuracies in the radius. As result, the air gap does not match the preferable uniform height of 1.0 mm and is non-uniform. Especially, at both ends of the SLIM the air gap is significantly bigger than in the middle. The average air gap height will be determined with help of the analytical and numerical models, thus via backward-fitting of the air gap.

The primary is attached to a four degrees of freedom (4 DoF) piezoelectric force sensor. The Kistler 9272 force sensor consists of a quartz four-component dynamometer that measurers the torque T_z and the three orthogonal components of force F_x, F_y and F_z. The Kistler 9272 sensor has a

great rigidity and, consequently, a high natural frequency, its high resolution enables the smallest dynamic changes in large forces and torques to be measured. Table III shows the most important characteristics of the Kistler 9272 dynamometer. The maximum normal force F_z will not exceed 500 N, with help of (39) the resonance frequency $f_{z_{res}}$ will be approximately equal to 958 Hz at maximum force:

$$f_{z_{res}} = \frac{1}{2\pi}\sqrt{\frac{c_z}{\left(M_{Kistler} + \frac{F_z}{G}\right)}}, \qquad (39)$$

where G denotes the gravitational acceleration.

TABLE III
CHARACTERISTICS OF KISTLER 9272 FORCE SENSOR

	symbol	value	unit
Range	F_x, F_y	-5 …5	kN
	F_z	-5 …20	kN
	M_z	-200 …200	Nm
Max. bending moment	M_x, M_y	-400 …400	Nm
Stiffness	c_x, c_y	0.4	kN/μm
	c_z	2	kN/μm
	c_{M_z}	70	Ncm/μrad
Natural frequency	$f_o(x,y)$	4	kHz
	$f_o(z)$	7	kHz
	$f_o(M_z)$	5	kHz
Weight	$M_{Kistler}$	4.2	kg

Although the force cell is optimally calibrated, there still exist small force errors. Table IV shows the errors introduced by the force cell and due to crosstalk between the x- and z-force components. One should note the difference between the measured and given crosstalk of $F_x \rightarrow F_z$, fortunately the thrust forces will be significantly lower than normal forces, so this influence stays minimal. The influence of crosstalk has been taken into account for the measurement data shown in Section VI. The static test setup is constructed very stiff, as can be seen in Fig. 7, because it should be able to bear hundreds of Newtons.

TABLE IV
CALIBRATION ERRORS

vector	error [%] measured	error [%] datasheet 9272
F_x	0.270	$\leq$ | 0.3 |
F_z	-0.346	$\leq$ | 0.3 |
vectors	crosstalk [%] measured	crosstalk [%] datasheet 9272
$F_x \rightarrow F_z$	-8.235	-1.60
$F_z \rightarrow F_x$	-0.875	-0.50

The measurement setup, shown in Fig. 8, can schematically be divided into nine blocks. Initially, the reference frequency and reference RMS values of the three phase current I_{prim} are determined and implemented in ControlDesk of dSPACE. Frequency values from 0 till 200 Hz are swept across RMS current values from 4.15 till 6.8 A. The AC Power Amplifier (ACPA) has a bandwidth of 400 Hz and can maximally generate a RMS current of 6.8 A. The actual current RMS values are measured with a current probe. The charge amplifier

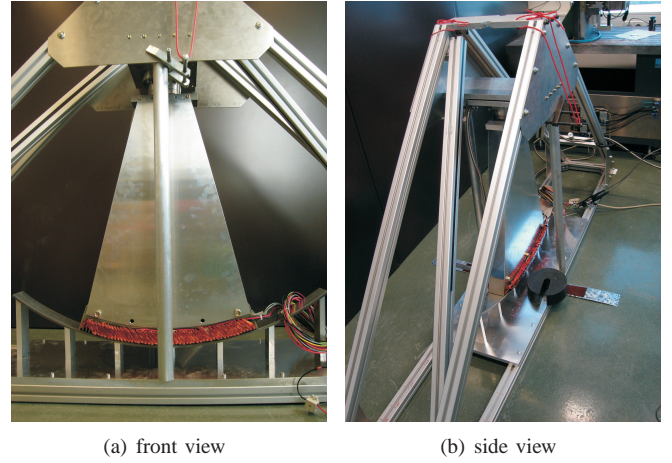(a) front view   (b) side view

Fig. 7.   The static test setup shown in: (a) front view and (b) side view.

(the Kistler 5019) is a 4-channel microprocessor system for converting the charges yield by the piezoelectric force sensor into proportional voltages. These voltages are passed through to the DSPT SigLab 20-42, a four channel dynamic signal analyzer with a 16-bit resolution. A SCSI cable connects the DSPT with a laptop that runs SigLab software, all SigLab software applications are written in MATLAB. This makes it easy to apply MATLAB's computational power for any post-processing requirements. The virtual oscilloscope of SigLab has a timebase of 195.3 μs/sample and a record length of 5120 samples. Multiple measurements have been taken per frequency per RMS current value.
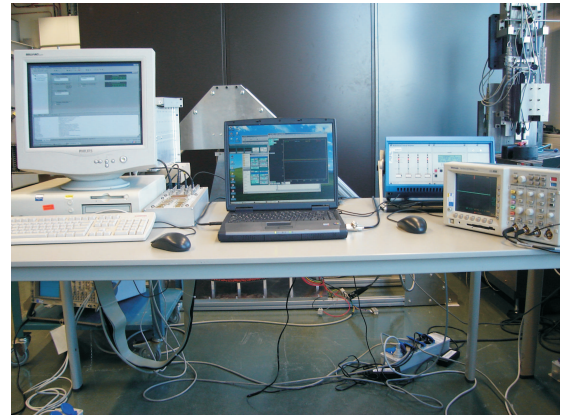
(a) measurement setup
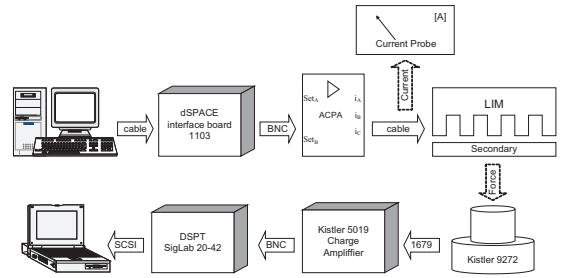
(b) block diagram of measurement setup

Fig. 8.   Measurement setup illustrated in: (a) photo and (b) block diagram.
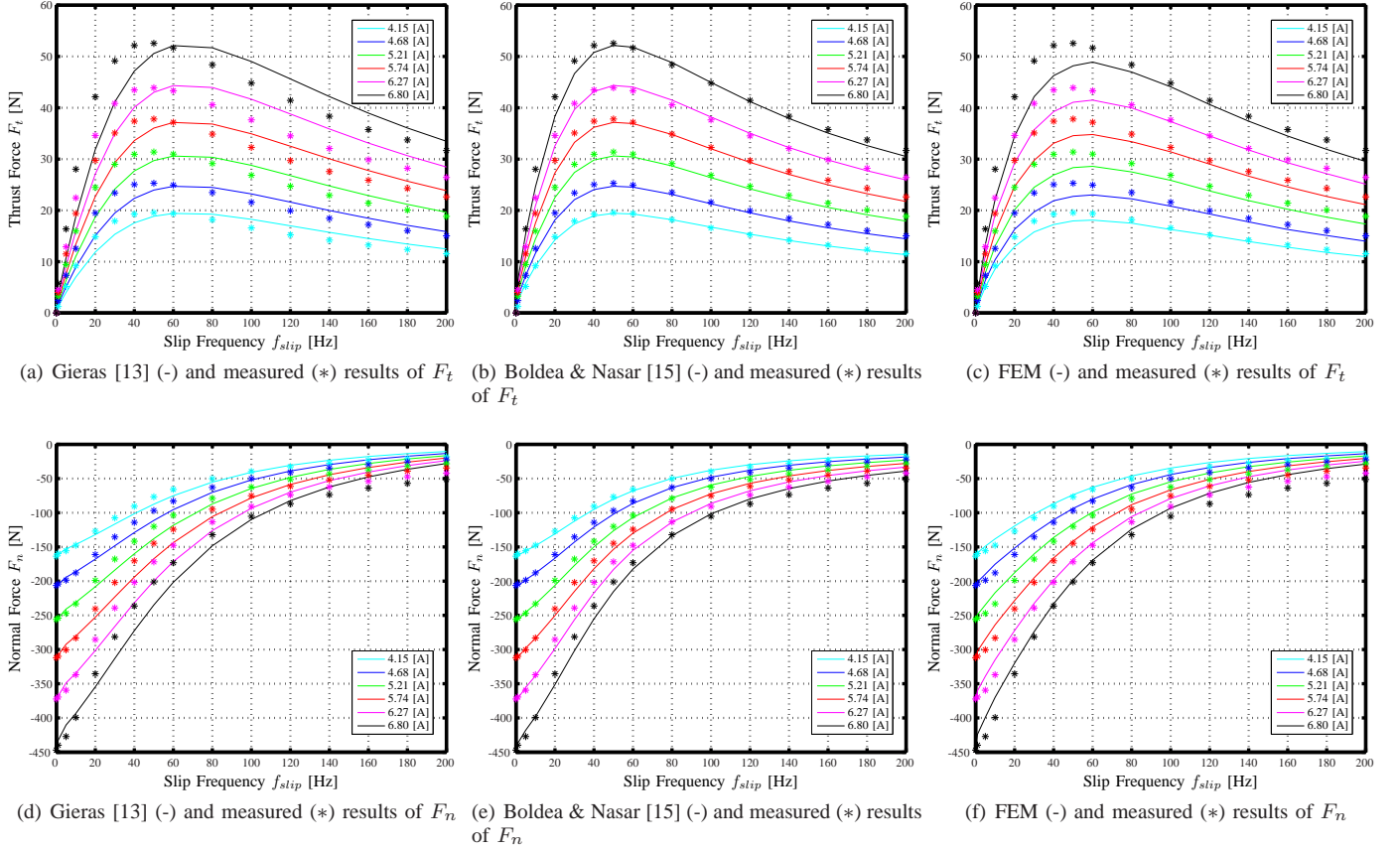
(a) Gieras [13] (-) and measured (∗) results of F_t

(b) Boldea & Nasar [15] (-) and measured (∗) results of F_t

(c) FEM (-) and measured (∗) results of F_t

(d) Gieras [13] (-) and measured (∗) results of F_n

(e) Boldea & Nasar [15] (-) and measured (∗) results of F_n

(f) FEM (-) and measured (∗) results of F_n

Fig. 9. The measurement results (∗) and the Gieras [13], Boldea & Nasar [15] and FEM results (-) respectively shown for the thrust forces F_t (a), (b), (c) and the normal forces F_n (d), (e) and (f).

VI. RESULTS

As stated in Section V, the air gap g of the three models will be determined with the backward-fitting method. The normal force F_n at zero slip frequency f_{slip} is fitted on the measured F_n at zero f_{slip}. The conductivity, and thus the transverse edge effect, has no influence at this frequency, Table V gives the fitted air gap per model.

TABLE V

BACKWARD-FITTING OF AIR GAP PER MODEL

Model	Air gap [mm]
Gieras [13]	1.38
Boldea & Nasar [15]	1.20
FEM	1.20

The results can be seen in Fig. 9. One should notice Boldea & Nasar's model coincides the most with the measurements. There are two reasons why the numerical results of FEM are lower than the measured ones. Both reasons are the result of the 2D-origin of the model; the first one is due to the transverse edge effect which lowers the σ_{Al}, and the second one is due to the same interpreted 70 mm width of the primary L_{prim} and secondary w_{sec}. However, from Table I one could see L_{prim} and w_{sec} are respectively equal to 70 mm and 80 mm. With help of Gieras' model the influence of the width of the primary and secondary is shown and illustrated in Fig. 10. This figure

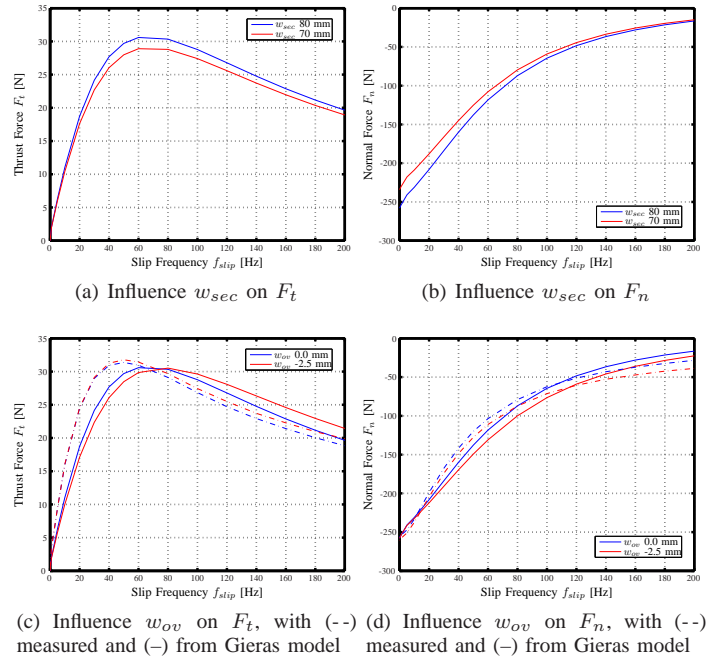clearly shows why FEM has lower force calculation results than the measured ones.

(a) Influence w_{sec} on F_t

(b) Influence w_{sec} on F_n

(c) Influence w_{ov} on F_t, with (- -) measured and (–) from Gieras model

(d) Influence w_{ov} on F_n, with (- -) measured and (–) from Gieras model

Fig. 10. Influence of (a) w_{sec} on thrust force F_t, (b) w_{sec} on normal force F_n, (c) w_{ov} on thrust force F_t and (d) w_{ov} on normal force F_n at 5.21 A.

Due to a construction error, the width of the Aluminum layer was in the beginning shorter than the width of the secondary back iron w_{sec}. However, Fig. 10 shows interesting information about w_{ov}, the width of the Aluminum layer with respect to w_{sec}, and its influence on the force performance.
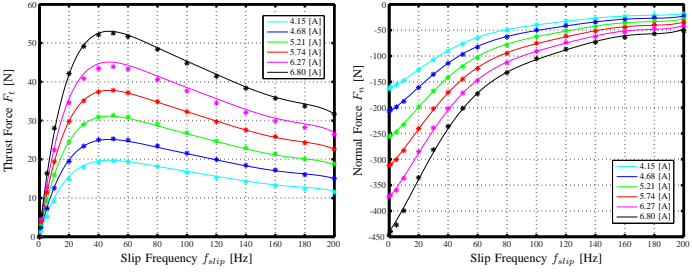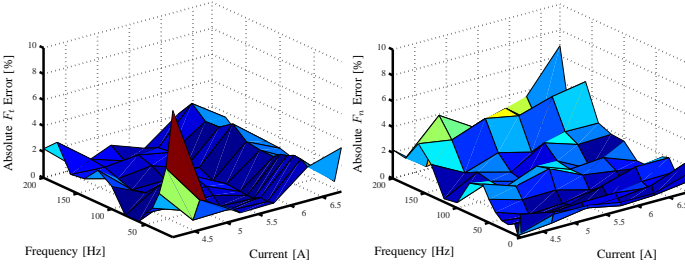

(a) Fit (-) and measured ($*$) results of F_t

(b) Fit (-) and measured ($*$) results of F_n
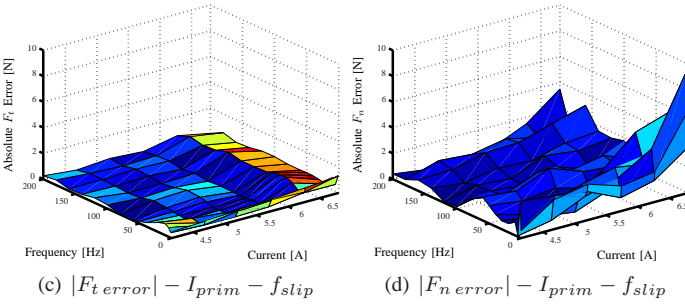
(c) $|F_{t\,error}| - I_{prim} - f_{slip}$

(d) $|F_{n\,error}| - I_{prim} - f_{slip}$

(e) $F_{t\,error}|\%| - I_{prim} - f_{slip}$

(f) $F_{n\,error}|\%| - I_{prim} - f_{slip}$

Fig. 11.   Thrust and normal forces analysis.

A fit, based on least squares, has been made on thrust force F_t and normal force F_n according to:

$$\mathbf{F} = \sum_{i=0}^{6} \left(a_i f_{slip}^i\right) I_{prim}^2. \tag{40}$$

According to (40) it follows that if there is no magnetic saturation, the thrust and normal forces are approximately a function of the squared primary current. Four remarks have to be discussed based on the results of Fig. 11.

First of all, Figs. 11(c) and 11(e) show an error offset at a current value of 6.27 A for every frequency. Because there is no reason to assume the force error increases proportionaly with the current, it can be concluded that it appears to be an inaccurate measurement. A lot of factors can heavily influence the measurements, for example; the air gap height, the SLIM temperature and the drift of the force sensor.

Secondly, Fig. 11(e) shows an error percentage peak at 4.15 A at lower frequencies, this can be clarified by a very low

value of measured thrust force.

Thirdly, there exists a peak at 0 Hz and 6.8 A in Fig. 11(d). The high normal force at this low frequency and high current result in an air gap displacement of the SLIM caused by the finite stiffness of the measurement setup. This introduces an even higher measured normal force, nevertheless, the absolute error is less than 1.44 %.

Finally, Fig. 11(f) shows significant occuring errors at 160 and 200 Hz, but the frequency range beyond 60 Hz is out of consideration which will be treated in Section VII.

VII. SYSTEM ARCHITECTURE

The rotating ring system consists of two primaries, SLIM A and SLIM B, which are respectively placed under an angle of α_a and α_b, as illustrated in Fig. 12. The magnetic bearings in the axial direction consists of an array of PMs, with help of OPERA-2D dimensions of the PMs were derived to satisfy a predefined axial stiffness of $8.3 \cdot 10^6$ N/m.
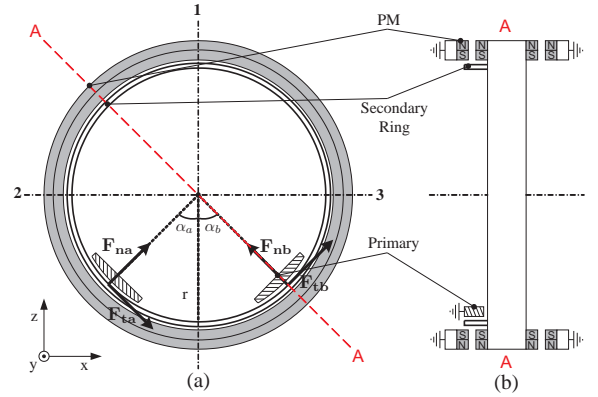

Fig. 12.   (a) Front view of the total system architecture of the rotating ring setup and (b) the cross-section A-A through the red (- -) line.

One should note that the thrust force in Fig. 12 can independently be controlled in either the positive or negative tangential direction per SLIM. The following constraints have been defined to successfully rotate and magnetically levitate the ring:

$$F_z = MG, \tag{41}$$

$$F_x = 0, \tag{42}$$

$$F_{na} \text{ and } F_{nb} \leq 0, \tag{43}$$

$$\alpha = \alpha_a = \alpha_b, \tag{44}$$

with M-the total mass of the ring and G-the gravitational acceleration. Position **1** in Fig. 12 denotes where an E-core should be placed to control the air gap. For an even more mechanically stable system E-cores should be placed at positions **2** and **3**. E-cores, or active magnetic bearings, have already been studied in [20].

Figure 13 illustrates the torque control scheme of the overall rotating ring system, where $\star$ denotes reference value. This system does not take into account control of the air gap, but it delivers a pre-tension of the ring. A motion profile is processed by the controller which produces a reference torque $T_y^\star$. With
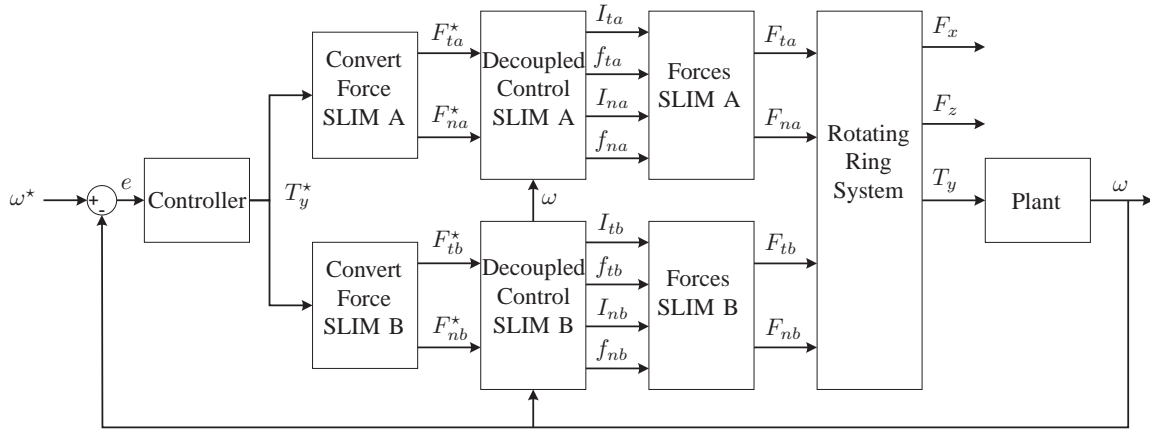
Fig. 13.   Torque control scheme of overall rotating ring system.

the total architecture and the four constraints of (41-44) in mind, the four reference forces can be derived. The four forces are built up from eight variables, namely four currents and four frequencies. The plant consists of the dynamics of the ring with inclusion of damping due to core losses and air flow resistance.
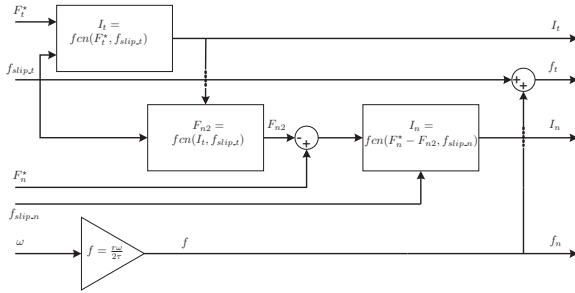

Fig. 14.   Decoupled control of normal and thrust forces per SLIM.

The intelligence of this system is implemented in block 'Decoupled Control SLIM', explicitly shown in Fig. 14, which calculates the values of respectively the thrust and normal RMS currents and frequencies per SLIM. First, the optimal slip frequencies have to be derived. If the results of Section VI are used, one should conclude from Figs. 11(a) and 11(b) that f_{slip_t} and f_{slip_n} are equal to 50 and 0 Hz respectively. Therefore, frequencies above 60 Hz are out of consideration. The thrust current I_t, derived from the inverse fit function, will simultaneously produce a normal force F_{n2}. Subtraction of this force from the reference normal force $F_n^\star$ leads to the calculation of the normal current I_n. The mechanical frequency f of the ring is the same as the normal frequency f_n, because f_{slip_n} is set at 0 Hz.

The number of pole pairs p per SLIM has been increased from 4 to 8, as result, the force performance significantly improves and withstands the mass M of the ring without saturation of currents. The forces, with the air gap g of 1 mm, have been calculated with help of OPERA-2D and a fit has been made on these results. Finally, the two SLIMs are placed under an angle α of $40°$ and the results from Simulink are shown in Fig. 15. The angle α of $40°$ is chosen to fulfill

sufficient ring space between the two SLIMs. In other words, the ring space between the two SLIMs is sufficient enough to have no influence of induced eddy currents from one SLIM to the other [18]. As stated before, the air gap is controlled by the E-core at position **1**. Using this E-core as part of pre-tension, results in significant lower primary currents than shown in Fig. 15. As result, smaller SLIMs with less number of poles could be implemented in the total system architecture.
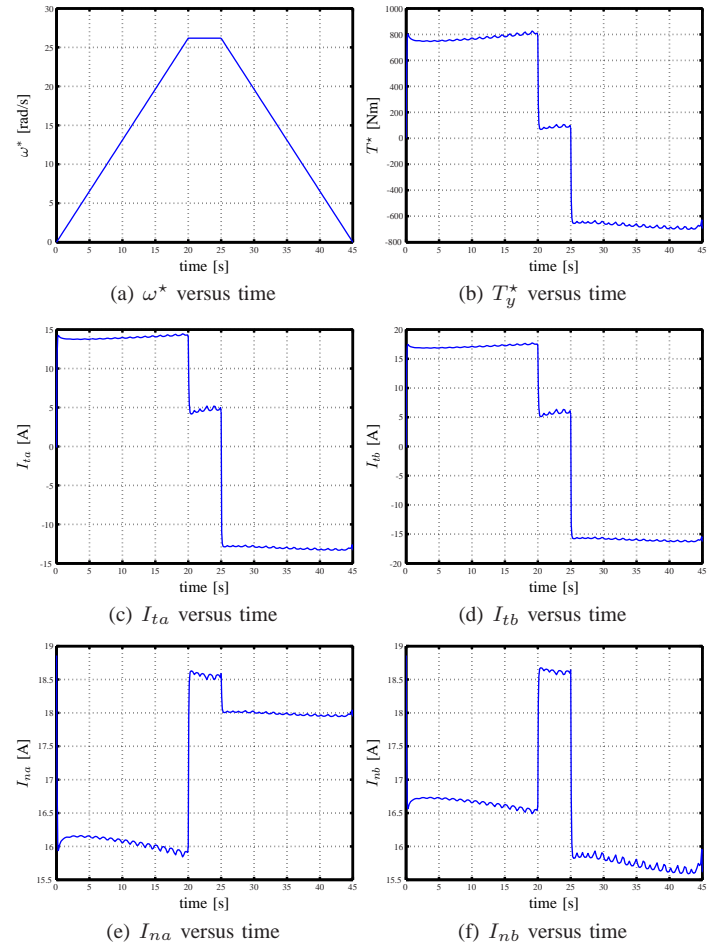

(a) $\omega^\star$ versus time

(b) $T_y^\star$ versus time

(c) I_{ta} versus time

(d) I_{tb} versus time

(e) I_{na} versus time

(f) I_{nb} versus time

Fig. 15.   Simulink results with (a) motion profile, (b) torque profile, (c) and (d) thrust current profiles, and (e) and (f) normal current profiles.

VIII. Conclusions & Recommendations

This paper has shown a novel method of simultaneous and decoupled control of thrust and normal forces of the SLIM for a new magnetically levitated system. The results of this novel method are very promising and the following conclusions and recommendations can be drawn.

Analytical and numerical models have been created to capture the physical phenomena and force performance of the SLIM. Model comparison shows significant correlation of the thrust and normal forces as function of the slip frequency, although, force values differ per model.

A static test setup has been designed and constructed to gain measured force results. Due to a non-uniform and unknown value of the air gap, these models are backward-fitted on the air gap height. It can be concluded that Boldea & Nasar's model coincides the most with the measurements of the static test setup.

The FEM values are slightly lower than the measurements due to the two dimensionality of the software, a 3D FEM AC model would include the finite widths and the transverse edge effects. Although the analytical and FEM models have been designed for a linear shaped SLIM, the influence of the arc-shaped SLIM could easily be studied with a FEM model.

An analytical fit has been made on the measurements, which is independent of the air gap height of the SLIM. The fit proves that saturation does not exist for the used current values. The frequencies of interest for thrust and normal force are respectively 0 and 50 Hz, the absolute error for all current values is less than 2.60% for thrust and 1.44% for normal force.

Because more thrust and normal force is produced with a smaller width of the Aluminum layer, further investigation related to this topic is required.

Additionally, the novel method to decouple simultaneously the thrust and normal forces has been implemented. It excels in simplicity and straightforwardness, making it an easy to build in method. The intelligence of this method lies in the fact that the thrust force producing current simultaneously generates a normal force. The normal force producing current is set at zero slip frequency, which means it does not produce thrust force.

Besides, a preliminary study has been carried out in respect with the dynamical test setup. The magnetic positioning in the axial direction is performed by an array of PMs, the dimensions are derived from FEM and ensure a stiffness of $8.3 \cdot 10^6$ N/m in axial direction.

The final step should be to construct and accomplish the dynamical setup. Firstly, the E-cores should be used to control the air gap and give information about the behavior of the SLIM. Secondly, a conclusion should be drawn whether the E-cores are desirable to control the air gap or only to give an pre-tension against gravity force. This influences the demanded forces, thus the amplitude of the currents and the length of the SLIMs. The created models have already been included with motion parasitic effects, so verification between the results of the models and dynamical test setup should be performed.

References

[1] A.K.Rathore and S.N.Mahendra, "Simulation of secondary flux oriented control of linear induction motor considering attraction force & transverse edge effect," *9th IEEE International Power Electronics Congress*, pp. 158–163, 17-22 October 2004.

[2] J.H.Sung and K.Nam, "A new approach to vector control for a linear induction motor considering end effects," *IEEE Industry Applications Conference, Thirty-Fourth IAS Annual Meeting*, vol. 4, pp. 2284–2289, 3-7 October 1999.

[3] G.Kang and K.Nam, "Field-oriented control scheme for linear induction motor with the end effect," *IEE Proc. Electr. Power Appl.*, vol. 152, pp. 1565–1572, November 2005.

[4] P. E.F. da Silva, E.B. dos Santos and M. de Oliveira, "Vector control for linear induction motor," *IEEE International Conference on Industrial Technology*, vol. 1, pp. 518–523, 10-12 December 2003.

[5] P. E.F. da Silva, E.B. dos Santos and M. de Oliveira, "Dynamic model for linear induction motor," *IEEE International Conference on Industrial Technology*, vol. 1, pp. 478–482, 10-12 December 2003.

[6] A.K.Rathore and S.N.Mahendra, "Decoupled control of attraction force and propulsion force in linear induction motor drive," *IEEE International Conference on Industrial Technology*, vol. 1, pp. 524–529, 10-12 December 2003.

[7] N. T.Morizane and K.Taniguchi, "Simultaneous control of propulsion and levitation of linear induction motor in a novel maglev system," *IEEE Third International Power Electronics and Motion Control Conference PIEMC 2000*, vol. 1, pp. 127–131, 15-18 August 2000.

[8] L. K.Yosshida and T.Yoshida, "Decoupled-control method of normal and thrust forces in linear induction motor for maglev vehicle marine-express me01," *IEEE International Conference IEMD on Electric Machines and Drives*, pp. 369–371, 9-12 May 1999.

[9] I.Takahashi and Y.Ide, "Decoupling control of thrust and attractive force of a lim using a space vector control inverter," *IEEE Transactions on Industry Appl.*, vol. 29, pp. 161–167, February 1993.

[10] T. K.Yoshida and K.Noda, "Influence of instantaneous end effects on attractive levitation force at standstill of combined-levitation-and-propulsion slim," *IEEE Sixth International Conference on Electrical Machines and Systems*, vol. 1, pp. 187–190, 9-11 November 2003.

[11] S.Yamamura, *Theory of Linear Induction Motors*. Tokyo, Japan: University of Tokyo Press, 1972.

[12] J.F.Gieras, *Linear Induction Drives*. New York: Oxford University Press Inc., 1994.

[13] G. J.F.Gieras and A.R.Eastham, "Performance calculation for single-sided linear induction motors with a solid steel reaction plate under constant current excitation," *IEEE Proceedings*, vol. 132, pp. 185–194, July 1985.

[14] G. J.F.Gieras and A.R.Eastham, "Performance calculation for single-sided linear induction motors with a double-layer reaction rail under constant current excitation," *IEEE Transactions on Magnetics*, vol. 22, pp. 54–62, January 1986.

[15] I.Boldea and S.A.Nasar, *Linear Motion Electromagnetic Systems*. New York: John Wiley & sons Inc., 1985.

[16] I.Boldea and S.A.Nasar, "A complete equivalent circuit of a linear induction motor with sheet secondary," *IEEE Transactions on Magnetics*, vol. 24, pp. 639–654, January 1988.

[17] F.Sahin and J.Compter, "Linear induction motor design overview," Tech. Rep. CTB534-05-2574, Philips Applied Technologies, Eindhoven, The Netherlands, 2005.

[18] A.J.D.Verdel, "Decoupled control of thrust and normal forces of linear induction motor for novel magnetically levitated system," Master's thesis, Eindhoven University of Technology, January 2007.

[19] G. K.Adamiak, J.Mizia and A.Eastham, "Finite element force calculation in linear induction machines," *IEEE Transactions on Magnetics*, vol. 23, pp. 3005–3007, September 1987.

[20] A.J.D.Verdel, "Active magnetic bearings," tech. rep., Philips Applied Technologies, San Jose, U.S.A., 2006.